Regulation of age-related macular degeneration-like pathology by complement factor H

Christopher B. Toomey[a,b], Una Kelly[a], Daniel R. Saban[a,c], and Catherine Bowes Rickman[a,b,1]

[a]Department of Ophthalmology, Duke Eye Center, Duke University, Durham, NC 27710; [b]Department of Cell Biology, Duke University, Durham, NC 27710; and [c]Department of Immunology, Duke University, Durham, NC 27710

Edited by Jeremy Nathans, Johns Hopkins University, Baltimore, MD, and approved April 28, 2015 (received for review December 19, 2014)

Complement factor H (CFH) is a major susceptibility gene for age-related macular degeneration (AMD); however, its impact on AMD pathobiology is unresolved. Here, the role of CFH in the development of AMD pathology in vivo was interrogated by analyzing aged *Cfh*$^{+/-}$ and *Cfh*$^{-/-}$ mice fed a high-fat, cholesterol-enriched diet. Strikingly, decreased levels of CFH led to increased sub-retinal pigmented epithelium (sub-RPE) deposit formation, specifically basal laminar deposits, following high-fat diet. Mechanistically, our data show that deposits are due to CFH competition for lipoprotein binding sites in Bruch's membrane. Interestingly and despite sub-RPE deposit formation occurring in both *Cfh*$^{+/-}$ and *Cfh*$^{-/-}$ mice, RPE damage accompanied by loss of vision occurred only in old *Cfh*$^{+/-}$ mice. We demonstrate that such pathology is a function of excess complement activation in *Cfh*$^{+/-}$ mice versus complement deficiency in *Cfh*$^{-/-}$ animals. Due to the CFH-dependent increase in sub-RPE deposit height, we interrogated the potential of CFH as a previously unidentified regulator of Bruch's membrane lipoprotein binding and show, using human Bruch's membrane explants, that CFH removes endogenous human lipoproteins in aged donors. Thus, advanced age, high-fat diet, and decreased CFH induce sub-RPE deposit formation leading to complement activation, which contributes to RPE damage and visual function impairment. This new understanding of the complicated interactions of CFH in AMD-like pathology provides an improved foundation for the development of targeted therapies for AMD.

age-related macular degeneration | retinal pigmented epithelium | complement | factor H | lipoprotein

Age-related macular degeneration (AMD) affects about 30% of Americans over age 70 (1–3) and is the leading cause of irreversible vision loss in the elderly in industrialized nations (4). It is a progressive, chorioretinal degenerative disease influenced by both environmental and genetic factors and is dependent upon advanced age (5, 6). Although the presence of a few small "hard" drusen is a normal, non–vision-impairing part of aging, the deposition of large diffuse drusen in the macula is vision impairing and indicative of early AMD. As AMD progresses to late-stage disease, it is categorized as either "dry" [geographic atrophy, with photoreceptor loss and extensive retinal pigmented epithelium (RPE) atrophy] or "wet" (exudative, with subsequent choroidal neovascularization) (7). Over the past decade, a large body of evidence has emerged that implicates the complement system in the pathogenesis and progression of AMD. For example, pathobiologic investigations have led to the identification of numerous complement proteins in drusen (8–10), and genetic studies have resulted in the discovery of variants in several complement genes that confer significant risk for, or protection from, the development of AMD late in life (11–16). In particular, the complement factor H (*CFH*) gene, where a nucleotide change results in a tyrosine (Y)-to-histidine (H) exchange in short consensus repeat 7 (amino acid 402), increases AMD risk dramatically (11, 13–15). CFH is the soluble inhibitor of the alternative pathway of complement, limiting formation of C3 convertase and acting as a cofactor to factor I which degrades C3b to inactive iC3b. It is now apparent that dysregulation of the complement cascade, and of the alternative pathway in particular (17, 18), is a critical predisposing step in AMD development.

Another major consequence of RPE–choroid pathology in AMD is the deposition and sequestration of cellular and acellular debris sub-RPE between the RPE and Bruch's membrane (BrM) that leads to drusen formation. BrM is a pentalaminar extracellular matrix between the RPE and choroid comprised of distinct sublamina containing collagen and elastin-based fibrous connective tissue elements and a variety of proteoglycans, including heparan sulfate-rich proteoglycans (19, 20). Lipoprotein particles accumulate in BrM with aging, before the development of sub-RPE deposits and drusen, as neutral lipids that are characterized by an abundance of esterified cholesterol that arise from RPE cells as components of apolipoprotein-B–containing (ApoB) lipoproteins (21, 22). There is also a systemic contribution of ApoB-100–containing lipoproteins, including low-density lipoproteins (LDLs), which appear to be particularly important for the retina (23). The accumulation of lipoproteins leads to formation of a lipid "wall" in the inner collagenous layer of BrM that is proposed to be the precursor of the lipoprotein-derived debris in AMD that forms the sub-RPE deposits clinically detected as drusen (24, 25). Cholesterol (esterified and unesterified) and its transporter, ApoE, are also major constituents of these lipid-rich, sub-RPE deposits in AMD (17). Lipoprotein deposits that accumulate in AMD can be oxidized (26) and have been shown to activate complement through the binding of C-reactive protein to oxidized LDL (27, 28), or by oxidation-specific neoepitopes rendering the modified LDL immunogenic (29, 30). However, the link between CFH, complement dysregulation, and lipoproteins in BrM has not been elucidated in vivo.

Significance

Age-related macular degeneration (AMD) affects approximately one-third of Americans over 70 and is characterized by lipoprotein-rich sub-retinal pigmented epithelium (sub-RPE) deposits. Substantial evidence has emerged that implicates complement factor H (CFH) in the pathogenesis of AMD. Here, we conduct an in vivo analysis to elucidate the role of CFH in AMD pathology. We show that (*i*) CFH and lipoproteins compete for binding in the sub-RPE extracellular matrix such that decreasing CFH leads to lipoprotein accumulation and sub-RPE deposit formation; and (*ii*) detrimental complement activation within sub-RPE deposits leads to RPE damage and vision loss. This new understanding of the complicated interactions of CFH in development of AMD-like pathology paves the way for identifying more targeted therapeutic strategies for AMD.

Author contributions: C.B.T., U.K., and C.B.R. designed research; C.B.T. and U.K. performed research; D.R.S. contributed new reagents/analytic tools; C.B.T., U.K., D.R.S., and C.B.R. analyzed data; and C.B.T., U.K., and C.B.R. wrote the paper.

The authors declare no conflict of interest.

Freely available online through the PNAS open access option.

[1]To whom correspondence should be addressed. Email: bowes007@duke.edu.

This article contains supporting information online at www.pnas.org/lookup/suppl/doi:10.1073/pnas.1424391112/-/DCSupplemental.

AMD is a late-onset, complex disease (31); therefore, to interrogate the contribution of CFH to the pathogenesis and pathobiology of AMD, we developed an animal model based on multiple factors known to contribute to AMD. We combined advanced age with perturbations in lipid metabolism and the alternative complement pathway. Specifically, we aged C57BL/6J (B6), $Cfh^{+/-}$, and $Cfh^{-/-}$ mice over 90 wk and then fed them a high-fat, cholesterol-enriched (HFC) diet for 8 wk to mimic the environmental cholesterol and oxidative stressors linked to AMD in Western societies (5, 32–35). This experiment revealed that CFH levels impact sub-RPE deposit formation in mice, but, interestingly, only old $Cfh^{+/-}$ mice fed the HFC diet develop subsequent characteristics of early AMD including the following: ocular complement dysregulation, increased sub-RPE deposit formation, and RPE morphological changes that culminated in partial degeneration of the photoreceptor outer nuclear layer (ONL) and significantly impaired scotopic visual function. In contrast, no changes were observed in RPE morphology, ONL thickness, and scotopic visual function in the $Cfh^{-/-}$mice fed an HFC diet compared with age-matched $Cfh^{-/-}$ on a normal diet, despite the accumulation of significant sub-RPE deposits. We demonstrate that the pathology detected in old $Cfh^{+/-}$ mice fed an HFC diet is a function of complement dysregulation and associated mononuclear phagocyte (MNP) recruitment to the back of the eye, versus complement deficiency in $Cfh^{-/-}$ animals. To explain the dramatic increase in sub-RPE deposit height following HFC diet in CFH-deficient mice (both $Cfh^{-/-}$ and $Cfh^{+/-}$), we show that CFH competes with accumulated endogenous lipoproteins for binding to aged BrM. We also show $Cfh^{-/-}$ mice lack a functional systemic and local complement system due to uninhibited C3 "tick over," which generates activated C3 by spontaneous hydrolysis of C3 to C3(H_20) (36). Thus, based on our studies, we propose a model of AMD pathogenesis regulated by CFH whereby (*i*) CFH and lipoproteins compete for binding to BrM where decreased CFH promotes lipoprotein accumulation and sub-RPE deposit formation with age and environmental stressors, and (*ii*) excess complement activation in sub-RPE deposits results in RPE dysfunction and subsequent visual function decline.

Results

Fluid-Phase Complement Dysregulation in Aged $Cfh^{+/-}$ Mice Versus Complement-Deficient $Cfh^{-/-}$ Mice. To systematically test the role of CFH in AMD pathogenesis and progression in vivo, we developed a model system based on age, CFH deficiency, complement dysregulation, and cholesterol/oxidative stress using wild-type B6, $Cfh^{+/-}$ and $Cfh^{-/-}$ mice aged to 2 y that were then switched from a normal rodent chow diet (ND) to a HFC diet for 8 wk. As reported previously (36), $Cfh^{+/-}$ mice have approximately one-half of the circulating plasma levels of CFH compared with B6 mice on either diet, whereas there is no detectable CFH in the plasma of $Cfh^{-/-}$ mice (Fig. 1*A*). CFH levels showed the similar genotype-dependent distribution in RPE/choroid tissue lysates (Fig. 1*B*).

As previously reported, we found that decreased levels of CFH in aged $Cfh^{+/-}$ mice fed either diet leads to a decrease in intact C3 in the plasma, with no measureable C3b (Fig. 1*C*) (36, 37). In contrast, there is no intact C3 in plasma of $Cfh^{-/-}$ mice due to immediate conversion of C3 to C3b (Fig. 1*C*). Normally, when the alternative pathway is activated by C3 cleavage, factor B (FB) binds to C3b and is subsequently cleaved by factor D to form the alternative pathway convertase, C3bBb. Strikingly, in $Cfh^{-/-}$ mice, FB is almost entirely consumed, whereas $Cfh^{+/-}$ and B6 mice have ample intact FB (Fig. 1*D*). To further verify the lack of intact C3 in the plasma of $Cfh^{-/-}$ animals as well as reduced C3 in $Cfh^{+/-}$ plasma, we used a sensitive and quantitative hemolytic assay for the measurement of intact, fully functional mouse C3 (38). As expected, $Cfh^{+/-}$ mice had approximately one-half of the intact C3 compared with wild-type B6 mice, further validating that the fluid-phase tick over of C3 is accelerated with CFH deficiency (Fig. 1*E*). In contrast, no hemolysis was detected in $Cfh^{-/-}$ plasma, indicating that all of the C3 in the $Cfh^{-/-}$ mouse was already cleaved (Fig. 1*E*). This effect was not rescued by the addition of CFH to the assay and could only be rescued with the addition of C3 (Fig. S1). These data clearly demonstrate that $Cfh^{+/-}$ mice have increased fluid-phase consumption/conversion of C3 due to the decreased CFH levels, compared with B6 controls. Furthermore, the data show that the total lack of CFH in the $Cfh^{-/-}$ mice accelerates the consumption/conversion of C3 and FB to the point that there are no intact downstream components of the alternative pathway detectable in the plasma.

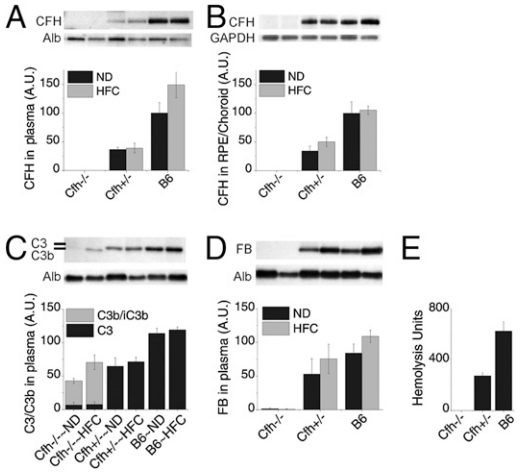

Fig. 1. Fluid-phase complement dysregulation in old $Cfh^{+/-}$ mice versus age-matched $Cfh^{-/-}$ mice, which are deficient in key activators of the complement cascade. (*A* and *B*) Densitometric analysis of CFH immunoblots from plasma (*A*) and lysates of RPE/choroid (*B*) across genotype and diet. Note that $Cfh^{+/-}$ mice have approximately one-half as much CFH as wild-type (B6) mice. (*C* and *D*) Densitometric analysis of C3/C3b (*C*) and FB (*D*) immunoblots from plasma of B6, $Cfh^{+/-}$ and $Cfh^{-/-}$ mice fed a normal (ND) or high-fat, cholesterol-enriched (HFC) diet. The dose effect of CFH on circulating C3 in plasma shows fluid-phase complement dysregulation in $Cfh^{+/-}$ mice, compared with B6 mice and the absence of circulating C3 and FB in $Cfh^{-/-}$ mice. (*E*) Red blood cell (RBC) hemolysis assay in each genotype; $Cfh^{+/-}$ mice had approximately one-half of the intact C3 compared with wild-type B6 mice, confirming fluid-phase complement dysregulation. In contrast, as expected, $Cfh^{-/-}$ mice were unable to lyse antibody-primed sheep RBCs due to the lack of reserve intact C3. Data are presented as mean ± SE. n = 5–8 per group. Albumin (Alb) served as a loading control in *A*, *B*, and *D*. GAPDH served as loading control in *C*.

Decreasing CFH Increases Sub-RPE Deposit Formation. Extracellular lesions that form between the RPE and BrM characterize early AMD (39–41). We used quantitative electron microscopy of RPE/BrM to analyze the height of similar sub-RPE deposits that accumulated in aged mice in response to *Cfh* genotype and diet. Sub-RPE deposit measurements were made from the elastic lamina of BrM (Fig. 2*A*, arrowhead) to top of deposits. Strikingly large (>4 μm) basal laminar deposits (BLamDs) (41) were often seen in the $Cfh^{+/-}$~HFC and $Cfh^{-/-}$~HFC mice, extending from the elastic lamina to the basal infoldings of the RPE (Fig. 2*A*). Deposits of this magnitude were absent in control B6~HFC mice. Vesicular structures with an electron-dense shell of 80–160 nm across were frequently observed (Fig. 2*A*, arrows) within a primarily amorphous deposit. The height of BLamD changed abruptly and varied from less than 0.2 μm to as much as 5.7 μm for a given section. Therefore, rather than estimating the amount of sub-RPE deposits per eye by examining a few transmission electron microscopy (TEM) images, we developed a method to systematically and objectively sample and measure the height or thickness of sub-RPE deposits by TEM (38). Using this method,

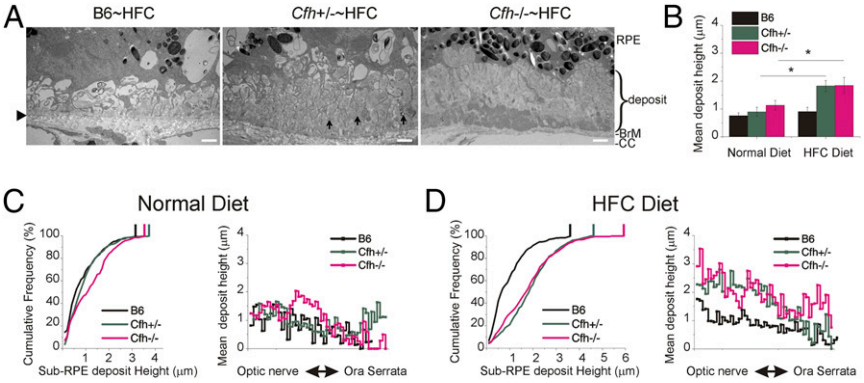

Fig. 2. Decreased CFH increases sub-RPE basal deposit load. (*A*) Transmission electron micrograph images of basal deposits along Bruch's membrane (BrM). Large (>4-μm height) deposits were often seen in the $Cfh^{+/-}$~HFC and $Cfh^{-/-}$~HFC BrM. Vesicular structures with an electron-dense shell of 80–160 nm across were also frequently observed (*A*, $Cfh^{+/-}$~HFC, arrows) within a primarily amorphous deposit. Arrowhead, elastic lamina of BrM. (Scale bars: 1 μm.) (*B*) ANOVA quantitative analysis was performed on the mean basal deposit height (n = 84–124 images per mouse) of each animal where the graph represents the mean ± SE across genotype and diet. Statistically significant increases in basal deposits were observed in the $Cfh^{+/-}$~HFC and $Cfh^{-/-}$~HFC mice. Asterisks indicate post hoc Tukey for a $P < 0.05$ following a statistically significant genotype by diet interaction by ANOVA. n = 6–8 mice per group. (*C* and *D*) Distribution of basal deposits for the three mouse genotypes fed a ND (*C*) or switched to a HFC diet (*D*) are represented by cumulative frequency curves showing the frequency of sub-RPE deposit heights (*Left*) and mean spatial distribution of sub-RPE deposit heights (*Right*). For the cumulative frequency plots, the genotype with the least number of deposits (B6, black trace) is represented by the curve that is furthest left (closest to the *y* axis). Vertical bars at the top of the cumulative frequency traces indicate the maximum deposit size for each genotype and diet combination. The cumulative frequency curves reveal a modest accumulation of basal deposits in the $Cfh^{-/-}$~ND, compared with the other genotypes on ND, but strikingly significant basal deposit accumulation occurs in both the $Cfh^{-/-}$ and $Cfh^{+/-}$ HFC fed animals and not in B6~HFC animals. Spatial distribution of sub-RPE deposits shows a central greater than peripheral decrease in sub-RPE deposit height following HFC diet (*D*, *Right*).

98 ± 18 (mean ± SD) images were taken per mouse eye from sections obtained from the center of the posterior eyecup near the optic nerve sampling from ora to ora.

Quantitative analysis of mean deposit height by genotype and diet demonstrated that sub-RPE deposits increased only in the mice fed a HFC diet that had reduced levels ($Cfh^{+/-}$~HFC) or no CFH ($Cfh^{-/-}$~HFC) ($P < 0.05$) (Fig. 2*B*). The distribution of sub-RPE deposit thickness was graphed by cumulative frequency and spatial distribution (Fig. 2 *C* and *D*). The cumulative frequency curve that is furthest to the left (closest to the *y* axis) in the plot represents the genotype with the least deposits (B6, black trace, Fig. 2 *C* and *D*, *Left*). The cumulative frequency plots revealed an inverse relationship between CFH levels and deposit load in the HFC-fed mice (Fig. 2*D*). In B6 and $Cfh^{+/-}$ mice fed a normal diet, very few deposits are seen, although there is some deposit accumulation in the $Cfh^{-/-}$ mice on normal diet as previously described (38) (Fig. 2*C*). Most strikingly, however, substantially more deposit was observed in $Cfh^{+/-}$~HFC and $Cfh^{-/-}$~HFC mice fed a HFC diet, whereas no increase in deposits was detected in the B6~HFC mice (Fig. 2). Furthermore, maximum deposit height is inversely related to CFH dose following HFC diet ($Cfh^{-/-}$ > $Cfh^{+/-}$ > B6) (Fig. 2*D*, *Left*, vertical bars). χ^2 statistical analysis shows that the increased frequency of large deposits seen in the $Cfh^{-/-}$~HFC mice is not due to chance, being significantly different from $Cfh^{+/-}$~HFC mice (>4.5 μm, $P < 0.05$; >5 μm, $P < 0.05$), even though the mean height is similar (Fig. 2*B*). The mean deposit height in the $Cfh^{+/-}$~HFC mice is diluted by more abundant smaller deposits (Fig. 2*D*, *Left*) so the maximum deposit size (top 5% of deposits) is not represented well in the mean analysis (Fig. 2*B*). Spatial distribution of sub-RPE deposits revealed the accumulation of sub-RPE deposit in the central retina is also inversely related to CFH levels following HFC diet (Fig. 2*D*, *Right*).

Attenuated Scotopic Visual Function in $Cfh^{+/-}$~HFC Mice. Visual function of the retinas of aged *Cfh* mice on and off a HFC diet was measured by scotopic electroretinogram (ERG), which primarily measures the rod photoreceptor function (42). Strikingly, visual function decline was only observed in $Cfh^{+/-}$ mice compared with the $Cfh^{-/-}$ and wild-type B6 mice after HFC diet (Fig. 3*A*). Similar trends shown for b-waves in Fig. 3 were also observed in the ERG a-waves (Fig. S2*A*). In addition, there were no measurable statistical changes in a/b-wave ratios, indicating that the attenuation of the b-wave responses originated in the photoreceptor (Fig. S2*B*) (43). Quantitative analysis of b-wave rod- and cone-driven responses was achieved by determining amplitude of Bmax1 (rod-dominant response; Fig. S2*C*) and Bmax2 (cone-dominant response; Fig. S2*D*). Analysis of variance showed that the 40% reduction in the rod-dominant response in $Cfh^{+/-}$ following HFC diet was statistically significant ($P < 0.05$), whereas the 22% reduction in cone-dominant response did not reach statistical significance. No statistically significant changes were detected among other genotype or diet interactions. These data were supported by a moderate (8.8%) but statistically significant ($P < 0.05$) reduction in photoreceptor ONL area in $Cfh^{+/-}$~HFC mice (Fig. S3). The data clearly show that $Cfh^{+/-}$ mice have a significant visual function decline following HFC diet, whereas wild-type and $Cfh^{-/-}$ mice do not.

RPE Damage in Aged $Cfh^{+/-}$~HFC Mice. To assess damage to the RPE cells in aged $Cfh^{+/-}$ and $Cfh^{-/-}$ mice resulting from exposure to the HFC diet, multinucleate RPE cells were quantified by immunostaining RPE flat mounts with the tight junction protein, zonula occludens-1 (ZO-1) (Fig. 3*B*) (44). Quantitative analysis showed that there is a small, but statistically significant, increase in multinucleate RPE cells (≥3 nuclei) in $Cfh^{+/-}$ mice compared with control B6 mice maintained on a ND. However, exposure to a HFC diet resulted in a large, statistically significant, increase in enlarged multinucleate RPE cells in the $Cfh^{+/-}$ mice [21.4 ± 2.8 (SE) versus 11.2 ± 1.4 (SE); $P < 0.05$] (Fig. 3*C*). In contrast, no detectable morphological differences in RPE were seen between wild-type and $Cfh^{-/-}$ mice in response to HFC diet (Fig. 3*C*). Damage to the RPE was further supported by the observation of RPE thinning in plastic sections of retina from $Cfh^{+/-}$~HFC mice (Fig. S4). Together, these data demonstrate RPE dysmorphogenesis in the $Cfh^{+/-}$~HFC mice, which is not detected in $Cfh^{-/-}$~HFC mice.

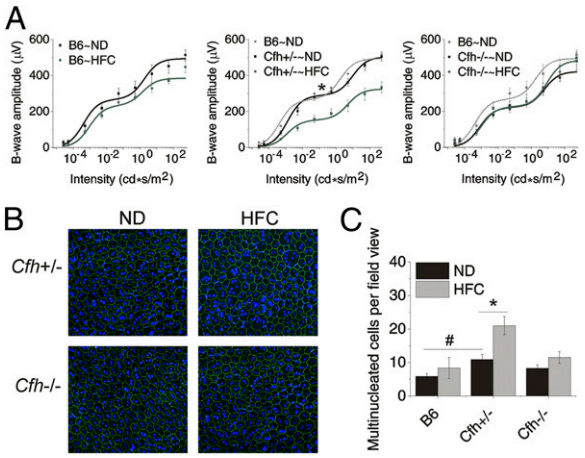

Fig. 3. Significant vision loss and RPE damage in response to the HFC diet is only detected in $Cfh^{+/-}$ mice. (*A*) Scotopic electroretinogram (ERG) flash responses in wild-type B6, $Cfh^{+/-}$ and $Cfh^{-/-}$ mice fed a ND or HFC diet. Stimulus–response curves of b-wave amplitudes. Data are expressed as mean ± SE of the stimulus–response curve overlaid with B = (Bmax1*I/I + I1)/(Bmax2*I/I + I2) comparing ND (black) to HFC (green) with B6~ND overlaid (gray in $Cfh^{+/-}$ and $Cfh^{-/-}$ graphs) for genotype comparisons. $Cfh^{-/-}$~ND mice were slightly worse at baseline compared with B6~ND and $Cfh^{+/-}$~ND mice; however, this failed to reach statistical significance by ANOVA. B6 and $Cfh^{-/-}$ mice showed no statistically significant depression of ERG amplitude with HFC diet. $Cfh^{+/-}$~HFC mice showed a marked decrease in b-wave amplitude (middle graph). The asterisk (*) indicates post hoc Tukey for a $P < 0.05$ following a statistically significant genotype by diet interaction by ANOVA for the mean Bmax1 value shown in Fig. S2. n = 6–10 mice per group. (*B*) Representative confocal fluorescence images of flat mounts of the central RPE from >90-wk-old mice $Cfh^{+/-}$ and $Cfh^{-/-}$ mice fed a ND or HFC diet that were stained with Hoechst 33342 (blue, nuclei) and anti-ZO-1 (green) and imaged RPE apical side up with the neural retina removed. In $Cfh^{+/-}$~HFC mice, there are many more enlarged, multinucleate cells. (*C*) Quantification of multinucleate (nuclei, ≥3) RPE cells per field view, demonstrating that $Cfh^{+/-}$~HFC RPE flat mounts have the largest number of multinucleate cells per field view of all of the groups. Data are presented as mean ± SE. The asterisk (*) indicates post hoc Tukey for a $P < 0.05$ following a statistically significant genotype by diet interaction by ANOVA. The number sign (#) indicates post hoc Tukey for a $P < 0.05$ following a statistically significant genotype interaction by ANOVA. n = 6–8 per group.

Local Ocular Deficiency of Key Complement Components in $Cfh^{-/-}$ Mice. Because sub-RPE deposits accumulated in both aged $Cfh^{+/-}$ and $Cfh^{-/-}$ mice fed the HFC diet, we sought to unravel why the $Cfh^{+/-}$ mice develop RPE dysmorphogenesis and visual function loss in response to HFC diet whereas the $Cfh^{-/-}$ animals do not. Based on the absence of intact C3 in the $Cfh^{-/-}$ plasma, we suspected a lack of complement activation in the BrM of $Cfh^{-/-}$~HFC mice, which would explain why there was no pathological response to the increased sub-RPE deposit formation in these mice. Western blot quantification of C3, C3b/iC3b (Fig. 4*A*), and FB (Fig. 4*B*) in the RPE/choroid revealed almost no intact C3, an absence of FB, and very little C3b/iC3b in $Cfh^{-/-}$ mice. C3 was also undetectable in BrM by immunohistochemistry in $Cfh^{-/-}$~HFC mice, whereas substantial C3 was localized to BrM of the $Cfh^{+/-}$~HFC mice (Fig. 4*C*). In contrast, $Cfh^{+/-}$~HFC mice have decreased C3 levels following HFC diet ($P < 0.05$) in the RPE/choroid (Fig. 4*A*), showing increased local C3 consumption/activation, as plasma C3 levels are unchanged (Fig. 1*C*). C3 consumption/activation is not seen following HFC diet in wild-type mice due to their abundance of CFH or in $Cfh^{-/-}$ animals due to their lack of C3. These results confirm that $Cfh^{-/-}$~HFC mice lack key activators of the complement cascade in the RPE and BrM and that local complement activation is occurring in $Cfh^{+/-}$~HFC mice.

Monocytosis and Increased Extravascular Monocytes in the RPE/Choroid of $Cfh^{+/-}$~HFC Mice. A major role of the complement system is the activation of the innate and adaptive immune systems by the complement cleavage products, C3a and, to a greater extent, C5a (45). As expected, increased C5a levels are detected in the plasma of $Cfh^{+/-}$~HFC mice compared with $Cfh^{-/-}$~HFC mice, further demonstrating the impairment of complement activation in $Cfh^{-/-}$ mice (Fig. S5). C5a has an established role in immune cell recruitment and has also been implicated in the development of atherosclerotic lesions (46–50). Significant populations of $CD11b^+$ myeloid cells were observed in the RPE/choroid near BrM by immunohistochemistry of $Cfh^{+/-}$~HFC mice, whereas $CD11b^+$ cells were rarer in $Cfh^{-/-}$~HFC mice and none could be found near the BrM and the RPE (Fig. 4*D*). Thus, we hypothesized that a functional consequence of dysregulated complement activation in the $Cfh^{+/-}$~HFC mice compared with the $Cfh^{-/-}$~HFC mice is enhanced MNP recruitment, which we tested by flow cytometry. In the peripheral blood, an established gating strategy was used to determine the percentage of classical and nonclassical monocytes (Fig. S6*A*) (51, 52). We were unable to detect changes between either monocyte subpopulations in $Cfh^{-/-}$ mice with diet (Fig. 4*E*). In contrast, in $Cfh^{+/-}$ mice there was a 5.3-fold increase in classical monocytes (2.4% versus 12.8%) and a 2.5-fold increase (3.9% versus 9.8%) in nonclassical monocytes following HFC diet, both of which reached statistical significance by χ^2 analysis ($P < 0.05$). In addition, in wild-type mice, there was a 1.5-fold increase (5.1% versus 7.9%) and 2.6-fold increase (2.1% versus 5.5%) in classical and nonclassical monocytes, respectively, which was also significant by χ^2 analysis ($P < 0.05$) (Fig. 4*E*). Overall the $Cfh^{+/-}$~HFC mice had the largest population of classical (12.8%) and nonclassical (9.8%) monocytes of the three *Cfh* genotypes and this was statistically significantly higher than in $Cfh^{-/-}$~HFC animals for nonclassical monocytes (9.8% versus 4.1%; $P < 0.05$) and B6~HFC for both classical (12.8% versus 7.9%; $P < 0.05$) and nonclassical monocytes (9.8% versus 5.5%; $P < 0.05$) (Fig. 4*E*).

To further test our hypothesis that $Cfh^{+/-}$~HFC mice develop a complement response to sub-RPE deposits, which is not seen in $Cfh^{-/-}$~HFC mice, we investigated whether there was recruitment of MNP in the RPE/choroid. Due to the high vascularity of the choroid, fluid perfusion is not a sufficient means to flush intravascular cells from contaminating flow cytometry. Therefore, we injected anti-CD45 fluorescent-conjugated antibodies (CD45-IV) intravascularly 5 min before killing to distinguish cells located in the intravascular space from those in the extravascular space (Fig. S6*B*) (53). With this method, we were able to identify the presence of extravascular MNPs recruited to the RPE/choroid within our aged $Cfh^{+/-}$~HFC model and $Cfh^{-/-}$~HFC controls (Fig. S6*C*). MNP cells were increased in $Cfh^{+/-}$ mice following HFC diet ($P < 0.05$) but were unchanged in $Cfh^{-/-}$ mice (Fig. 4*F*, *Top*). Using Ly6C and CD64 to differentiate MNPs, three clear subpopulations could be identified within the RPE/choroid, a $Ly6C^{lo}$, a $Ly6C^{hi}$, and a $Ly6C^{int}$ $CD64^+$ population (Fig. S6*C*). The $CD64^+$ MNP subpopulation in the $Cfh^{+/-}$~HFC model represents the largest myeloid cell population, increasing 2.8-fold over ND controls (10.9% versus 3.9%; $P < 0.05$), whereas it is barely detectable in $Cfh^{-/-}$~HFC mice (Fig. 4*F*, *Bottom*, and *H*, and Fig. S7*A*). Note that the $CD64^+$ subpopulation is significantly higher in $Cfh^{+/-}$~HFC mice compared with B6~HFC and $Cfh^{-/-}$~HFC mice (Fig. 4*G* and Fig. S7*A*). Further analysis showed that the $CD64^+$ MNP population has elevated expression of F4/80 and MHC class II, whereas the other myeloid cell populations detected did not (Fig. S7*B*). In addition, $CD64^+$ MNPs could not be found in peripheral blood or the choroidal intravascular space (Fig. S7*C*). Together, these findings help to establish the absence of a complement-mediated effector response to sub-RPE deposits in the $Cfh^{-/-}$~HFC mice.

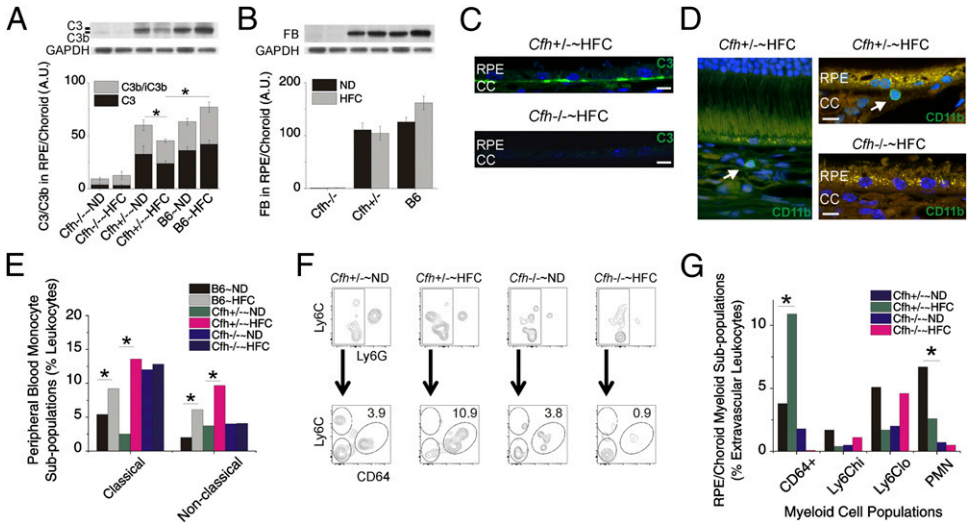

Fig. 4. Complement activation, monocytosis, and increased extravascular CD64$^+$ mononuclear phagocytes (MNPs) in *Cfh*$^{+/-}$~HFC mice versus local deficiency of key complement components in *Cfh*$^{-/-}$ mice. (*A* and *B*) Densitometric analysis of C3 (*A*) and FB (*B*) immunoblots in the RPE/choroid across genotype and diet. *Cfh*$^{-/-}$ mice have almost no detectable levels of intact C3, only minimal detectable C3b/iC3b, and no detectable levels of FB in the RPE/choroid lysates, whereas *Cfh*$^{+/-}$ mice have significant intact C3 and show a statistically significant decrease in intact C3 following HFC diet ($P < 0.05$), which is not seen in wild-type B6 or *Cfh*$^{-/-}$ mice. Data are presented as mean ± SE. $n = 6$–8 per group. (*C*) Anti-C3 (green) immunohistochemistry with Hoechst 33342 (blue, nuclei) staining of posterior eyecups. The 100× images at the RPE/BrM interface show no detectable C3 that can be localized to BrM, where sub-RPE deposit formation occurs in *Cfh*$^{-/-}$~HFC mice, whereas in *Cfh*$^{+/-}$~HFC mice significant amounts of C3 can be detected in BrM. $n = 3$ mice per group. (Scale bars: 5 μm.) (*D*) Immunolocalization of myeloid cells by anti-CD11b (green, arrow) near the BrM of posterior eyecups of *Cfh*$^{+/-}$~HFC mice plus Hoechst 33342 (blue, nuclei) staining. No anti-CD11b–positive cells were found near the RPE/BrM in the *Cfh*$^{-/-}$~HFC mice. (Scale bars: 5 μm.) (*E*) Classical and nonclassical monocyte populations were identified by Ly6C and CD43 gating as shown in Fig. S6*A*. A statistically significant 5.3-fold increase ($P < 0.05$) in classical monocytes was detected in *Cfh*$^{+/-}$~HFC mice in response to diet; in contrast, *Cfh*$^{-/-}$ have a baseline increase in classical monocytes, but no change was observed in *Cfh*$^{-/-}$~HFC mice, whereas B6 mice show a 1.5-fold increase ($P < 0.05$). Nonclassical monocytes showed a distinct, statistically significant, 2.5-fold increase ($P < 0.05$) in *Cfh*$^{+/-}$~HFC mice, which was not observed in *Cfh*$^{-/-}$~HFC mice but was also observed to a lesser extent in B6 mice ($P < 0.05$). Note that *Cfh*$^{+/-}$~HFC mice represent the largest population of classical (12.8%) and nonclassical (9.8%) monocytes in all genotypes. To assess RPE/choroid monocyte populations, intravascular flow cytometry analysis was performed as shown in Fig. S6 *B* and *C*. (*F*, *Top*) MNPs were increased in *Cfh*$^{+/-}$ mice following HFC diet but were unchanged in *Cfh*$^{-/-}$ mice. (*F*, *Bottom*) Three clear MNP populations were evident in the extravascular space a Ly6C^{hi}, a Ly6C^{lo}, and a CD64$^+$ population. (*G*) Note that the CD64$^+$ subpopulation in *Cfh*$^{+/-}$~HFC animals represents the largest myeloid cell population [CD64$^+$, Ly6C^{hi}, Ly6C^{lo}, and polymorphic neutrophils (PMN)] across all genotypes and diets within the study. The statistical significance of the MNP population changes was determined by using a χ^2 test for $P < 0.05$. The asterisk (*) indicates a statistically significant diet interaction. Data shown represent a pooled analysis of six mice per group. GAPDH served as a loading control in *A* and *B*.

CFH Levels Regulate Lipoprotein Binding in BrM and Remove Endogenous Lipoproteins in Human BrM. Our results demonstrate that sub-RPE deposit formation occurs in a CFH-dependent manner that is independent of increased complement activity, immune cell recruitment, RPE dysfunction, and visual function decline. These findings provide a proof of concept that lipoproteins can be retained in mouse, if the right retention matrix is present. Because mouse does not form basal linear deposit (a layer rich in lipoproteins in inner BrM), we tested these ideas further in human eye samples. In mouse, lipoproteins can be retained in the absence of CFH and suggested a previously unidentified direct function of CFH as a regulator of sub-RPE deposit formation. We hypothesized that CFH regulates lipoprotein deposit formation, accumulation of which in BrM is proposed to be the precursor of the lipoprotein-derived debris that forms the sub-RPE deposits (24, 25). Specifically, we hypothesized that CFH plays a direct role in competing with lipoproteins for binding to heparan sulfate proteoglycans (HSPGs) because lipoproteins interact with heparan sulfate (54), which is the main binding partner for CFH in human BrM (55, 56). Based on our in vivo observations, we performed a series of experiments using heparin binding columns and both young porcine and aged human BrM tissue to test the hypothesis that decreasing CFH increases lipoprotein binding to BrM HSPGs. Heparin-Sepharose columns were used to show that, although CFH competes with lipoproteins for binding to heparin (Fig. S8*A*), albumin does not (Fig. S8*B*). To further test our hypothesis in an ex vivo setting, we determined the range of concentrations of CFH that could bind to a 6-mm biopsy punch of BrM/choroid isolated from a young pig eye (Fig. 5*A*). We show that the EC_{50} of this interaction is 1 μM, establishing the specificity and affinity of the interaction (Fig. 5*A*). We then added a fixed amount of lipoproteins with increasing concentrations of CFH to these porcine explants and determined that by increasing the concentration of CFH we could dramatically reduce the binding of lipoprotein to the tissue (Fig. 5*B*). The use of heparin binding columns and young porcine BrM tissue are advantageous due to the absence of endogenous lipoprotein deposition, allowing control over lipoprotein deposition. In a final experiment, we validated the interaction using endogenous human BrM lipoproteins from aged human donors (Fig. 5 *C* and *D*). To test the interaction of CFH and endogenous human BrM lipoproteins, RPE/BrM/choroid punches obtained from aged (>75 y of age) human donor eyes were incubated overnight with or without 1 μM CFH (Fig. 5 *C* and *D*). Immunohistochemical analysis of human BrM explants showed that although some endogenous CFH exists in untreated RPE/BrM preparations (Fig. 5*C*, *Top*), following overnight incubation in 1 μM human CFH, CFH accumulates significantly above endogenous levels in BrM (Fig. 5*C*, *Bottom*). FPLC fractionation of human BrM lysates shows that 1 μM CFH removes endogenous very low density lipoprotein sized particles (fractions 15–17) from human BrM (Fig. 5*D*). Together, these results provide a mechanistic link that explains the increased sub-RPE deposit formation and accumulation detected in vivo in animals with decreased CFH.

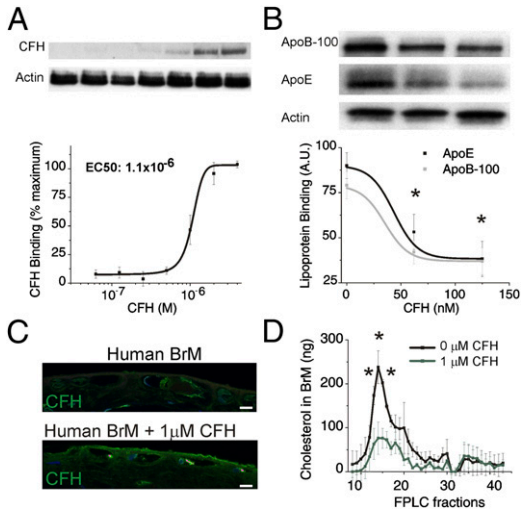

Fig. 5. CFH levels regulate lipoprotein binding and remove endogenous human lipoproteins in BrM. (*A* and *B*) Six-millimeter porcine RPE/BrM tissue explants were incubated with doubling concentrations of CFH (62 nM to 4 μM) in the presence of a 200 μM excess of albumin. (*A*) The amount of CFH bound to the tissue explant was determined by Western blot of the tissue lysate to determine EC_{50} binding. (*B*) Similar porcine tissue explants were incubated 2 μL of lipoprotein and increasing concentrations of CFH (0, 60, 120 nM), and lipoprotein binding to the explants was assessed by Western blot analysis for ApoB-100 and ApoE. Data are expressed as mean ± SE. The asterisk (*) indicates $P < 0.05$ for ApoE and ApoB-100 by ANOVA compared with 0 nM CFH. Data presented are a representative experiment from three independent experiments (n = 12–15). (*C*) Because aged human BrM contains endogenous sub-RPE lipoproteins, we tested the ability of CFH to remove these accumulated lipoproteins ex vivo. Anti-CFH (green) immunohistochemistry of aged human BrM donor tissue, before (*Top*) and after (*Bottom*) overnight incubation with 1 μM exogenous CFH, shows accumulation of CFH in BrM. (Scale bar: 5 μm.) (*D*) FPLC fractionation of human BrM lysates shows endogenous lipoproteins present in aged BrM tissue are removed with the addition of CFH (1 μM CFH, green trace). The asterisk (*) indicates $P < 0.05$ for total cholesterol in each fraction comparing 0 μM CFH to 1 μM CFH. Three independent experiments each with an $n = 3$ were performed to confirm these results of human BrM FPLC experiments. Actin served as a loading control in *A* and *B*.

Discussion

Our ability to unravel the link between complement dysregulation and the pathobiology of AMD has been hindered by the lack of a model that faithfully reconstitutes the multifactorial pathophysiology of AMD. Clearly, an important factor is CFH, where polymorphisms are responsible for a large fraction of the genetic attributable risk of AMD (11, 13–15, 57). Genetic polymorphisms, biochemical analysis of drusen, and clinical evidence have converged to strongly implicate CFH in having a role in the age-related progression to AMD (11, 13–15, 18). The use of aged $Cfh^{-/-}$ mice was expected to model the age-related progression of AMD pathogenesis (58). However, the absence of CFH in these mice leads to the rapid consumption of C3 and the development of severe membranoproliferative glomerulonephritis type II kidney disease often resulting in death between 12 and 24 mo of age in $Cfh^{-/-}$ mice (36). Animals that survive to 2 y have a mild retinal pathology including photoreceptor loss and reduced ERG (58). In $Cfh^{-/-}$ mice, C3 is cleaved as fast as it is generated; thus, neither intact C3 nor FB can be detected in the plasma or locally in BrM. The mild retinal phenotype that is observed can be explained by the absence of intact C3, which has a known role in regulating synaptic pruning both in development and in disease states (59). This idea is supported by data showing that the double-transgenic $Cfh^{-/-}$, $C3^{-/-}$ retinal phenotype is similar to the phenotype observed in $C3^{-/-}$ or $Cfh^{-/-}$ mice (60). In contrast, the $Cfh^{+/-}$~HFC mice we have characterized here display a robust AMD-like ocular phenotype, with substantial sub-RPE deposit formation, multinucleate RPE and atrophy, photoreceptor cell loss, and visual function decline (61, 62). It should be noted that nearly 10% of sub-RPE deposits were greater than 4 μm in height, which represents the largest deposits detected in any AMD mouse model within our laboratory; comparisons to other studies is difficult due to the lack of systematic quantification and the use of younger mice (38, 58, 60, 63–71). Data indicate that RPE damage and visual function loss in the $Cfh^{+/-}$~HFC model is initiated by sub-RPE deposit formation, primarily based upon the findings that $Cfh^{-/-}$~HFC mice develop substantial sub-RPE deposits without subsequent damage to the RPE and photoreceptors and that age-matched wild-type mice, which have an intact complement system, barely develop RPE deposits or damage to their RPE and photoreceptors. Thus, our data show that sub-RPE deposit formation occurs with the combination of diet and CFH deficiency before RPE/photoreceptor dysfunction. Furthermore, it is important to note that the cornerstones of the $Cfh^{+/-}$~HFC model are predominant factors established within the human disease: advanced age, genetic alteration of CFH, complement dysregulation, and cholesterol/lipid metabolism perturbation (15, 61, 62).

Characterization of the AMD-like phenotype in the $Cfh^{+/-}$~HFC mouse model also revealed a previously unidentified role for CFH in regulating the pathogenesis of sub-RPE deposit formation. A recent study uncovered a function for CFH in blocking the damaging effects of the lipid peroxidation product, malondialdehyde (72). Both Weismann et al. (72) and Shaw et al. (73) describe the ability of CFH to bind to chemically modified LDL, either malondialdehyde-acetaldehyde LDL (MAA-LDL) or $CuSO_4$ modified oxidized LDL (oxLDL), with much higher affinity than unmodified LDL. This binding prevents the detrimental inflammatory effects that the oxidized epitopes can potentiate. Our work focuses on the interaction of CFH and endogenous BrM lipoproteins and demonstrates that the amount of deposit—rather than the pathological effects of the deposit—appears to be regulated by CFH. In a series of experiments using aged BrM tissue and RPE cultures, Curcio et al. (22) identified 60- to 80-nm RPE-derived lipoproteins that accumulate in BrM with age, forming a "lipid wall" in BrM that is hypothesized to be the precursor to basal linear deposits and eventually visible on fundoscopic examination as drusen. Because the main binding partner for CFH in human macular BrM is heparan sulfate (55, 56) and lipoproteins interact with heparan sulfate (54), we hypothesized that CFH competes with lipoproteins for binding to HSPGs. This hypothesis is further supported by the high concentrations of HSPGs found in BrM as well as studies implicating HSPGs in AMD (55, 56, 74–76). Here, we show that CFH plays a direct role in modulating the interaction between BrM and endogenous lipoprotein particles that accumulate with age in human BrM. These lipoproteins resemble, in size, the RPE-derived lipoprotein-like particles described by Curcio et al., which are hypothesized to play a major role in the formation of the lipid wall and drusen biogenesis (22, 77, 78). Human studies support our hypothesis, as variants in CFH are related to the presence and progression of drusen in early AMD, suggesting that CFH is involved in early drusen formation in AMD (79). Future studies will be aimed at investigating the role of CFH variants and HSPGs in regulating BrM sub-RPE deposit formation (80, 81).

The size and number of drusen is diagnostic for early AMD and has a clinically predictive value for the progression to late-stage AMD where RPE atrophy occurs and visual acuity is significantly affected. Although sub-RPE deposit formation has been well established in AMD, the relationship between the deposition of sub-RPE debris and the development of the RPE and photoreceptor pathology in AMD has not been established. Our data show that $Cfh^{+/-}$~HFC and $Cfh^{-/-}$~HFC mice both

accumulate significant sub-RPE deposits in response to HFC diet but only $Cfh^{+/-}$~HFC mice have RPE and photoreceptor dysfunction in response to this extracellular debris. This difference between the two observed ocular phenotypes can be explained by the lack of a reservoir of intact C3 in $Cfh^{-/-}$~HFC mice. We hypothesize that sub-RPE deposits form at an accelerated rate in $Cfh^{-/-}$~HFC mice compared with normal age-matched controls (B6~HFC) due to the lack of CFH; however, in the absence of C3 and FB, no subsequent complement activation occurs, thus failing to initiate recruitment of MNPs. These MNPs may be the root cause of RPE dysfunction, as seen in a series of experiments using monocyte/RPE coculture systems. Elner and colleagues (82–85) have documented the pathological effects of monocytes on RPE cells. This hypothesis is supported by the absence of complement breakdown products, RPE/choroid monocyte recruitment, RPE damage, ONL thinning, and scotopic ERG attenuation, despite the significant sub-RPE deposit formation following HFC diet in $Cfh^{-/-}$ mice. Contrasting the abundance and absence of complement breakdown products in the $Cfh^{+/-}$~HFC and $Cfh^{-/-}$~HFC models, respectively, led us to investigate immune cell recruitment within the $Cfh^{+/-}$~HFC model due to the established role of C5a in immune cell recruitment (48). In addition, immune cell recruitment has been hypothesized to be a contributing factor to human AMD pathogenesis (18, 86). Evidence for monocyte involvement stems from analysis of genetic polymorphisms and immunohistochemical analysis of AMD postmortem tissue; however, the contribution of this immune cell recruitment to the disease phenotype had not been defined (87–93). Using the $Cfh^{+/-}$~HFC model, we established the presence of both a classical and nonclassical monocytosis in the blood following HFC diet. We were able to distinguish a significant, exclusive increase in a $CD11b^{+}$, $CD64^{+}$, $F4/80^{+}$, $I\text{-}A/E^{+}$ MNP subpopulation in $Cfh^{+/-}$~HFC choroid, which we suspect to be a monocyte-derived macrophage population. Furthermore, $CD11b^{+}$ myeloid cells could be localized near the BrM in the choroid of $Cfh^{+/-}$~HFC mice. Future studies will be aimed at investigating the role of specific complement breakdown products in local inflammation and monocyte recruitment and how these events affect the RPE and photoreceptor dysfunction seen within the $Cfh^{+/-}$~HFC model to develop therapies that block the progression of AMD following sub-RPE deposit formation.

Here, we establish the $Cfh^{+/-}$~HFC model as an aged, multifactorial, complement-dysregulated model of AMD with a robust ocular phenotype. This model provides evidence that complement activation, associated with MNP recruitment, is required for subsequent AMD-like pathology following sub-RPE deposit formation. Our discovery of CFH as a competitor for lipoprotein binding to BrM demonstrates, for the first time to our knowledge, that CFH has a pivotal role in sub-RPE deposit formation. Based on our studies we propose a model of AMD pathogenesis that is regulated by CFH whereby (*i*) CFH and lipoproteins compete for binding to heparan sulfate in BrM, leading to lipoprotein accumulation and sub-RPE deposit formation; and (*ii*) detrimental complement activation within sub-RPE deposits leads to recruitment of MNPs, RPE damage, and visual function decline. This new understanding of the complicated interactions of CFH in development of AMD-like pathology paves the way for identifying more targeted therapeutic strategies for AMD.

Materials and Methods

Mice. Mice were maintained in accordance with the Institutional Animal Care and Use Committee at Duke University. $Cfh^{+/+}$ (B6), $Cfh^{-/-}$, and $Cfh^{+/-}$ mice were generated as described (36). We have confirmed that none of the mice carries the rd8 mutation (94). Aged male B6, $Cfh^{+/-}$ and $Cfh^{-/-}$ mice (n = 84; 91–110 wk) were maintained on a normal rodent chow diet (ND) (Isopurina 5001; Prolab), and a subset of cage mate and littermate mice were switched to a HFC diet (n = 53; TD 88051; Harlan Teklad) for 8 wk. All mice were housed conventionally on a middle rack under ambient light conditions to control for light exposure. Mice were randomly assigned to treatment groups with an even distribution by age.

Western Blots Analysis for Quantification of FH, C3/C3b, and FB in Plasma and Tissue Lysates. Western blot analysis was performed as previously described (38). Briefly, plasma and RPE/choroid samples were diluted and run, nonreduced, on 10% (vol/vol) Bis-Tris Criterion XT gels in Mops buffer, transferred to nitrocellulose, and then probed with goat anti-FH (Quidel), goat anti-FB (Kent Laboratories), or rabbit anti-C3d (Dako). Loading controls for plasma and RPE/choroid were rabbit anti-albumin (Abcam) and mouse anti-GAPDH (Chemicon), respectively.

Hemolytic Assay for the Functional Measurement of Complement Activity in Mouse Plasma. Hemolytic assays were performed as previously described (38). Sheep red blood cells were coated with rabbit anti-sheep erythrocyte antiserum (Hemolysin). Six doubling dilutions of mouse plasma were added to a fixed amount of C3-depleted human serum and incubated for 1 h at 37 °C with the antibody-primed sheep erythrocytes. Ice-cold PBS with EDTA was added to stop the reaction, and tubes were spun at 1,811 × *g*, and optical density was measured at 412 nm. The reciprocal of the dilution for which 50% hemolysis was achieved gave the hemolytic units for that sample. Two hundred nanograms per microliter C3 and/or CFH was added to the reaction tubes for the experiment shown in Fig. S1.

In Vivo Visual Function Analysis by Electroretinography. Electroretinography was performed as previously described (38, 44). Briefly, mice were dark-adapted overnight, pupils dilated with 0.5% tropicamide and 1.25% (wt/vol) phenylephrine, and anesthetized with a mixture of ketamine (100 mg/kg) and xylazine (10 mg/kg). Scotopic ERGs were recorded using an Espion E2 system (Diagnosys), at increasing flash intensities. The data points from the b-wave stimulus–response curves were fitted according to a previously published equation using the least-square fitting procedure (43) (OriginPro 9.0; OriginLab). Statistical significance was determined using the mean values for Bmax1 and Bmax2.

Quantification of Sub-RPE Deposits by Electron Microscopy. Quantification of sub-RPE deposits was performed as previously described (38). Briefly, thin sections of 60–80 nm were cut from embedded sections of central retina starting at the optic nerve, collected onto 400 mesh thin-bar copper grids (T400-Cu; Electron Microscopy Sciences), and stained with Sato's lead. Images containing the basal RPE and BrM were taken on the parts of the section adjacent to the grid's bar. Using this method, 98 ± 18 (mean ± SD) images were taken per mouse, sampling most of the retina. For each image, the height of the sub-RPE deposits was measured using ImageJ software (version 1.46; NIH), and the cumulative frequency and spatial distribution of the deposit height was plotted using OriginPro 9.0 software.

Analysis of RPE Damage Based on Flat-Mount Quantification of Multinucleate Cells. RPE flat-mount preparation was performed as previously described (44). Briefly, flat mounts of RPE cells were stained with a rabbit antibody against ZO-1 (40-2200; 1:100; Invitrogen) and Hoechst 33342, and confocal images were captured on a Nikon Eclipse C1 microscope. Morphometric analysis was performed by a masked grader from each central quadrant. The number of multinucleated (nuclei, ≥3) cells per central field view was counted.

Quantification of ONL Thickness and Assessment of RPE Atrophy on Toluidine Blue Plastic Sections. ONL thickness was analyzed as previously described (38). Briefly, posterior eyes were osmicated, dehydrated with ethanol, infiltrated, and embedded in a mixture of epoxy and Spurr's resin. Semithin sections were cut superior to inferior, mounted, and stained with toluidine blue. The 40× images were merged with Photoshop, and ONL was measured versus distances from the optic nerve. Data are presented as ONL height versus distance from optic nerve. Inner nuclear layer (INL) thickness was also measured versus distance from the optic nerve, and ONL/INL area was used to control for angle of the plastic section cut, which was also statistically significant in $Cfh^{+/-}$ following HFC diet. For RPE height measurements, 100× sections were required; thus, field views were taken from the optic nerve to the ora serrata, and RPE cell height was averaged between the first and last possible RPE height measurement for each image, and this observation was presented as graph of the mean ± SE of RPE height for each field view from optic nerve. RPE height measurements were not an outcome measure of the original experiment and are thus not subject to postexperimental statistical analysis, but rather are presented as a quantitative observation.

Immunohistochemical Localization for C3 and CD11b. Immunohistochemistry for C3 and CD11b were done as previously described (38). Briefly, free-floating sections were blocked and incubated overnight with anti-mouse C3d (1:500; R&D Systems) or anti-mouse CD11b (1:500; Pierce), then incubated for 2 h in Alexa fluorophore-conjugated secondary antibody (1:500; Invitrogen), and counterstained with Hoechst 33342 (1:500, Invitrogen). Confocal images were acquired using a Ziess 710 inverted confocal microscope.

Anti-C5a ELISA. Briefly, 1 μg/100 μL anti-C5a (Pfizer; 4C9) was incubated at 4 °C overnight in 96-well plates. After washing unbound antibody and blocking with 1% BSA, a 1:50 dilution of plasma was incubated overnight at 4 °C. Following the wash steps, the plate was sequentially incubated with biotinylated rat anti-mouse C5a (BD Biosciences), streptavidin-peroxidase (Sigma), and TMB substrate reagent (BD Biosciences), and the OD at 450 nm was read. mC5a (R&D Systems) was used as a standard curve.

Peripheral Blood and Extravascular RPE/Choroid Monocyte Analysis with Flow Cytometry. Extravascular staining was performed with the following modifications to the previously published method (53). Five minutes before being killed, mice were injected retroorbitally with 3 μg/50 μL APC/Cy7 anti-mouse CD45 (BioLegend) (CD45-IV) in the right eye. Mice were then killed and perfused postmortem with 30 mL of PBS to wash unbound antibody from vasculature (53). Peripheral blood was analyzed as a positive (>90%) control of vascular localization (Fig. S6*B*) (53). Peripheral blood samples were subjected to RBC lysis and staining for cell viability (eBiosciences; 65-0863), CD45 (BioLegend; 110735), CD11b (BD Biosciences; 562950), CD115 (eBiosciences; 61-1152), CD43 (BD Pharmingen; 562866), Ly6C (BioLegend; 128022), and Ly6G (BioLegend; 127621) to determine the percentage of classical and nonclassical monocytes per $CD45^+$ cells based on established methods (Fig. S6*A*) (51). The left eye was enucleated and the RPE/choroid/sclera was isolated by microdissection. RPE/choroid was mechanically removed from the subadjacent sclera. Six eyes were pooled to obtain cell numbers sufficient for analysis. Samples then underwent DNase I and collagenase treatment with mechanical stimulation to free immune cells. Subsequently, samples were filtered and stained for cell viability, CD11b, CD45, Ly6C, Ly6G, CCR2 (R&D Systems; FAB5538A), CD11c (BD Biosciences; 563048), CD64 (BioLegend; 100539), F4/80 (BioLegend; 123109), and I-A/E (BioLegend; 107629). Using gating strategies established in other organs, we found that, using Ly6C and CD64, we could identify three clear subpopulations: $Ly6C^{lo}$, $Ly6C^{hi}$, and a $Ly6C^{int}$, $CD64^+$ population (Fig. S6*C*) (51, 52, 95, 96). χ^2 statistical test for $P < 0.05$ was used to determine the statistical significance of the cell population frequencies normalized to total extravascular $CD45^+$ cells for a pooled sample.

CFH and Lipoprotein Binding to Heparin-Sepharose Beads. Heparin-Sepharose columns (5-μL washed beads; GE Healthcare) were preincubated with increasing concentrations of CFH (prepared as previously described) (97) or albumin (0, 400, 800, and 1,600 nM) for 20 min at room temperature; after washing off excess protein, 2 μL of a lipoprotein preparation isolated from human donor blood using ultracentrifugation of human plasma adjusted to a specific gravity of 1.21 was added to all of the columns for an additional 20 min at room temperature. Following washing, the bound proteins were eluted with 1 M NaCl, and these fractions were run on 10% (wt/vol) Bis-Tris XT Criterion gels. One gel was stained by Coomassie and used to quantify (by densitometry and ImageJ) and identify [using a quantitative quadrupole time-of-flight mass spectrometer (Waters Synpt G2) with a liquid chromatography-MS/MS workflow], CFH, albumin, ApoB-100, and ApoA-1. The other gel was transferred to nitrocellulose, and Western blot analysis was used to measure ApoE (goat anti-human ApoE; Calbiochem).

Porcine RPE/BrM Lipoprotein/CFH Binding Assays. For porcine BrM experiments, human serum lipoproteins were isolated as described above. BrM explants were isolated as previously described (97). Porcine eyes were chosen because they have little to no BrM lipid accumulation and show low background for anti-human ApoB-100 and ApoE antibodies on a Western blot. EC_{50} values were determined by incubation of porcine BrM explants overnight in 10 mM PB with increasing concentrations of CFH (60 nM to 4 μM). Albumin at 200 μM was added to each sample to block nonspecific binding. Following five, 10-min washes in 10 mM PB, proteins were extracted, and Western blot analysis was performed using 1:5,000 goat anti-FH (Quidel) and an HRP-conjugated secondary as previously described using 25 ng of total protein lysate. The actin loading control had 5 μg of lysate per well, and these samples were diluted 1:200 to observe the CFH in the linear range (98). Data presented are a representative of two independent experiments (n = 4–8). For competition assays, a fixed amount of human lipoproteins (2 μL) with increasing concentrations of CFH (60 and 120 nM) was added overnight at 4 °C to 6-mm porcine explants in a well of a 96-well plate. After five, 10-min washes in 10 mM PB, proteins were extracted, and Western blot analysis was performed using 1:30,000 goat anti–ApoB-100 (EMB Millipore), 1:5,000 goat anti-ApoE (CalBiochem), and 1:3,000 mouse anti-Actin (Santa Cruz) primary antibodies and an HRP-conjugated secondary as previously described (38). Data are expressed are a representative experiment of three independent experiments (N = 12–15).

Aged Human RPE/BrM Endogenous Lipoprotein/CFH Competition Assays. Human donor eyes were obtained from the North Carolina Eye Bank. Due to the previously described age-related accumulation of lipoproteins in human BrM, eyes from donors >75 y of age were used for this study (99–101). RPE/BrM punches were isolated as previously described (97), and then were randomly assigned to incubation overnight at 4 °C in 200 μL of 10 mM PB with or without 1 μM CFH. Following incubation, the tissue was washed in 10 mM PB five times. For immunohistochemistry, tissue was fixed with 4% (wt/vol) paraformaldehyde for 20 min, and then washed with PBS for overnight storage. Tissue was embedded in 10% (wt/vol) low melting temperature agarose (Sigma-Aldrich) and 70-μm vibratome sections were cut. Immunohistochemistry staining was performed as previously described (38). For lipoprotein analysis, 80 μL of RIPA buffer with protease inhibitors and mechanical homogenization was used to isolate lipoproteins. Homogenates were pooled, and 50 μL was run on an FPLC system (Pharmacia LKB) with a Superose 6HR 10/30 column (GE Healthcare), and 40, 500-μL fractions were collected. Total cholesterol was determined for each fraction by enzymatic cholesterol assay (Amplex Red Cholesterol Kit; Invitrogen). Data are expressed as a pooled n = 3. Three independent experiments have been performed.

Statistical Analysis. ANOVA statistical analysis with post hoc Tukey test for $P > 0.05$ was used to determine the statistical significance of the mean effects for the 3 × 2 (genotype by diet) interaction term experimental design. Following a detection of a statistically significant genotype by diet interaction, post hoc Tukey test comparing ND to HFC for each genotype was used to determine the statistical significance of diet on each genotype. Following detection of a statistically significant genotype effect, post hoc Tukey test was performed comparing B6~ND to the experimental genotypes $Cfh^{+/-}$~ND and $Cfh^{-/-}$~ND and designated by the number sign (#) (Fig. 3*C* and Fig. S3*C*). For CFH binding assays, an ANOVA statistical analysis was used. Statistical analyses were performed in JMP Pro-9 software.

ACKNOWLEDGMENTS. We thank Jindong Ding, Mikael Klingborn, Nikolai Skiba, Terry Singhapricha, and Marybeth Groelle for their expert technical assistance; Rose Matthews and Joan Kalnitsky for their assistance with flow cytometry; Scott Cousins, Dan Stamer, Christine Curcio, Lincoln Johnson, and Ekaterina Lobanova for their intellectual contributions to the manuscript; and Marina Botto for access to the $Cfh^{-/-}$ mice. This work was supported by funding grants from the National Eye Institute [P30 EY005722 (to V. Arshavsky), R01 EY019038 (to C.B.R.), and T32 GM007171–Medical Scientist Training Program (to C.B.T.)], an unrestricted grant from Research to Prevent Blindness (to the Duke Eye Center), and a grant from the Edward N. and Della L. Thome Memorial Foundation (to C.B.R.).

1. Jager RD, Mieler WF, Miller JW (2008) Age-related macular degeneration. *N Engl J Med* 358(24):2606–2617.
2. Klein R, Klein BE, Linton KL (1992) Prevalence of age-related maculopathy. The Beaver Dam Eye Study. *Ophthalmology* 99(6):933–943.
3. Vingerling JR, et al. (1995) The prevalence of age-related maculopathy in the Rotterdam Study. *Ophthalmology* 102(2):205–210.
4. Klein BE, Klein R, Lee KE (2002) Incidence of age-related cataract over a 10-year interval: The Beaver Dam Eye Study. *Ophthalmology* 109(11):2052–2057.
5. Chen W, et al.; Complications of Age-Related Macular Degeneration Prevention Trial Research Group (2010) Genetic variants near TIMP3 and high-density lipoprotein-associated loci influence susceptibility to age-related macular degeneration. *Proc Natl Acad Sci USA* 107(16):7401–7406.
6. Strittmatter WJ, et al. (1993) Apolipoprotein E: High-avidity binding to β-amyloid and increased frequency of type 4 allele in late-onset familial Alzheimer disease. *Proc Natl Acad Sci USA* 90(5):1977–1981.
7. Penfold PL, Madigan MC, Gillies MC, Provis JM (2001) Immunological and aetiological aspects of macular degeneration. *Prog Retin Eye Res* 20(3):385–414.
8. Anderson DH, Mullins RF, Hageman GS, Johnson LV (2002) A role for local inflammation in the formation of drusen in the aging eye. *Am J Ophthalmol* 134(3):411–431.
9. Johnson LV, Leitner WP, Staples MK, Anderson DH (2001) Complement activation and inflammatory processes in drusen formation and age related macular degeneration. *Exp Eye Res* 73(6):887–896.
10. Johnson LV, Ozaki S, Staples MK, Erickson PA, Anderson DH (2000) A potential role for immune complex pathogenesis in drusen formation. *Exp Eye Res* 70(4):441–449.

11. Edwards AO, et al. (2005) Complement factor H polymorphism and age-related macular degeneration. *Science* 308(5720):421–424.
12. Gold B, et al.; AMD Genetics Clinical Study Group (2006) Variation in factor B (BF) and complement component 2 (C2) genes is associated with age-related macular degeneration. *Nat Genet* 38(4):458–462.
13. Hageman GS, et al. (2005) A common haplotype in the complement regulatory gene factor H (HF1/CFH) predisposes individuals to age-related macular degeneration. *Proc Natl Acad Sci USA* 102(20):7227–7232.
14. Haines JL, et al. (2005) Complement factor H variant increases the risk of age-related macular degeneration. *Science* 308(5720):419–421.
15. Klein RJ, et al. (2005) Complement factor H polymorphism in age-related macular degeneration. *Science* 308(5720):385–389.
16. Yates JR, et al.; Genetic Factors in AMD Study Group (2007) Complement C3 variant and the risk of age-related macular degeneration. *N Engl J Med* 357(6):553–561.
17. Anderson DH, et al. (2001) Local cellular sources of apolipoprotein E in the human retina and retinal pigmented epithelium: Implications for the process of drusen formation. *Am J Ophthalmol* 131(6):767–781.
18. Anderson DH, et al. (2010) The pivotal role of the complement system in aging and age-related macular degeneration: Hypothesis re-visited. *Prog Retin Eye Res* 29(2): 95–112.
19. Booij JC, Baas DC, Beisekeeva J, Gorgels TG, Bergen AA (2010) The dynamic nature of Bruch's membrane. *Prog Retin Eye Res* 29(1):1–18.
20. Call TW, Hollyfield JG (1990) Sulfated proteoglycans in Bruch's membrane of the human eye: Localization and characterization using cupromeronic blue. *Exp Eye Res* 51(4):451–462.
21. Curcio CA, Johnson M (2013) Structure, function, and pathology of Bruch's membrane. *Retina*, ed Ryan SJ (Elsevier, Philadelphia), 5th Ed, Vol 1, pp 465–481.
22. Curcio CA, Johnson M, Rudolf M, Huang JD (2011) The oil spill in ageing Bruch membrane. *Br J Ophthalmol* 95(12):1638–1645.
23. Tserentsoodol N, et al. (2006) Uptake of cholesterol by the retina occurs primarily via a low density lipoprotein receptor-mediated process. *Mol Vis* 12:1306–1318.
24. Curcio CA, Johnson M, Huang JD, Rudolf M (2009) Aging, age-related macular degeneration, and the response-to-retention of apolipoprotein B-containing lipoproteins. *Prog Retin Eye Res* 28(6):393–422.
25. Ruberti JW, et al. (2003) Quick-freeze/deep-etch visualization of age-related lipid accumulation in Bruch's membrane. *Invest Ophthalmol Vis Sci* 44(4):1753–1759.
26. Yamada Y, et al. (2008) Oxidized low density lipoproteins induce a pathologic response by retinal pigmented epithelial cells. *J Neurochem* 105(4):1187–1197.
27. Chang MK, Binder CJ, Torzewski M, Witztum JL (2002) C-reactive protein binds to both oxidized LDL and apoptotic cells through recognition of a common ligand: Phosphorylcholine of oxidized phospholipids. *Proc Natl Acad Sci USA* 99(20):13043–13048.
28. Binder CJ, et al. (2002) Innate and acquired immunity in atherogenesis. *Nat Med* 8(11):1218–1226.
29. Hörkkö S, et al. (2000) Immunological responses to oxidized LDL. *Free Radic Biol Med* 28(12):1771–1779.
30. Zhou HF, et al. (2012) Antibody directs properdin-dependent activation of the complement alternative pathway in a mouse model of abdominal aortic aneurysm. *Proc Natl Acad Sci USA* 109(7):E415–E422.
31. Swaroop A, Chew EY, Rickman CB, Abecasis GR (2009) Unraveling a multifactorial late-onset disease: From genetic susceptibility to disease mechanisms for age-related macular degeneration. *Annu Rev Genomics Hum Genet* 10:19–43.
32. Age-Related Eye Disease Study Research Group (2000) Risk factors associated with age-related macular degeneration. A case-control study in the age-related eye disease study: Age-Related Eye Disease Study Report Number 3. *Ophthalmology* 107(12):2224–2232.
33. Chakravarthy U, et al. (2010) Clinical risk factors for age-related macular degeneration: A systematic review and meta-analysis. *BMC Ophthalmol* 10:31.
34. McKay GJ, et al. (2011) Evidence of association of APOE with age-related macular degeneration: A pooled analysis of 15 studies. *Hum Mutat* 32(12):1407–1416.
35. Dashti N, McGwin G, Owsley C, Curcio CA (2006) Plasma apolipoproteins and risk for age related maculopathy. *Br J Ophthalmol* 90(8):1028–1033.
36. Pickering MC, et al. (2002) Uncontrolled C3 activation causes membranoproliferative glomerulonephritis in mice deficient in complement factor H. *Nat Genet* 31(4): 424–428.
37. Pangburn MK, Müller-Eberhard HJ (1983) Initiation of the alternative complement pathway due to spontaneous hydrolysis of the thioester of C3. *Ann N Y Acad Sci* 421: 291–298.
38. Ding JD, et al. (2015) Expression of human complement factor h prevents age-related macular degeneration-like retina damage and kidney abnormalities in aged cfh knockout mice. *Am J Pathol* 185(1):29–42.
39. Curcio CA, Millican CL (1999) Basal linear deposit and large drusen are specific for early age-related maculopathy. *Arch Ophthalmol* 117(3):329–339.
40. Green WR (1999) Histopathology of age-related macular degeneration. *Mol Vis* 5:27.
41. Sarks SH (1976) Ageing and degeneration in the macular region: A clinico-pathological study. *Br J Ophthalmol* 60(5):324–341.
42. Gouras P (1970) Electroretinography: Some basic principles. *Invest Ophthalmol* 9(8): 557–569.
43. Herrmann R, et al. (2010) Phosducin regulates transmission at the photoreceptor-to-ON-bipolar cell synapse. *J Neurosci* 30(9):3239–3253.
44. Ding JD, et al. (2011) Anti-amyloid therapy protects against retinal pigmented epithelium damage and vision loss in a model of age-related macular degeneration. *Proc Natl Acad Sci USA* 108(28):E279–E287.
45. Zipfel PF, Skerka C (2009) Complement regulators and inhibitory proteins. *Nat Rev Immunol* 9(10):729–740.
46. Ward PA (2009) Functions of C5a receptors. *J Mol Med (Berl)* 87(4):375–378.
47. Rittirsch D, et al. (2008) Functional roles for C5a receptors in sepsis. *Nat Med* 14(5): 551–557.
48. Guo RF, Ward PA (2005) Role of C5a in inflammatory responses. *Annu Rev Immunol* 23:821–852.
49. Manthey HD, et al. (2011) Complement C5a inhibition reduces atherosclerosis in ApoE$^{-/-}$ mice. *FASEB J* 25(7):2447–2455.
50. Skeie JM, Fingert JH, Russell SR, Stone EM, Mullins RF (2010) Complement component C5a activates ICAM-1 expression on human choroidal endothelial cells. *Invest Ophthalmol Vis Sci* 51(10):5336–5342.
51. Carlin LM, et al. (2013) Nr4a1-dependent Ly6C(low) monocytes monitor endothelial cells and orchestrate their disposal. *Cell* 153(2):362–375.
52. Hanna RN, et al. (2011) The transcription factor NR4A1 (Nur77) controls bone marrow differentiation and the survival of Ly6C- monocytes. *Nat Immunol* 12(8):778–785.
53. Anderson KG, et al. (2014) Intravascular staining for discrimination of vascular and tissue leukocytes. *Nat Protoc* 9(1):209–222.
54. Sarrazin S, Lamanna WC, Esko JD (2011) Heparan sulfate proteoglycans. *Cold Spring Harb Perspect Biol* 3(7):pii:a004952.
55. Clark SJ, et al. (2010) Impaired binding of the age-related macular degeneration-associated complement factor H 402H allotype to Bruch's membrane in human retina. *J Biol Chem* 285(39):30192–30202.
56. Clark SJ, et al. (2013) Tissue-specific host recognition by complement factor H is mediated by differential activities of its glycosaminoglycan-binding regions. *J Immunol* 190(5):2049–2057.
57. Fritsche LG, et al. (2013) Seven new loci associated with age-related macular degeneration. *Nat Genet* 45(4):433–439, 439e1–439e2.
58. Coffey PJ, et al. (2007) Complement factor H deficiency in aged mice causes retinal abnormalities and visual dysfunction. *Proc Natl Acad Sci USA* 104(42):16651–16656.
59. Stephan AH, Barres BA, Stevens B (2012) The complement system: An unexpected role in synaptic pruning during development and disease. *Annu Rev Neurosci* 35: 369–389.
60. Hoh Kam J, Lenassi E, Malik TH, Pickering MC, Jeffery G (2013) Complement component C3 plays a critical role in protecting the aging retina in a murine model of age-related macular degeneration. *Am J Pathol* 183(2):480–492.
61. Zeiss CJ (2010) Animals as models of age-related macular degeneration: An imperfect measure of the truth. *Vet Pathol* 47(3):396–413.
62. Pennesi ME, Neuringer M, Courtney RJ (2012) Animal models of age related macular degeneration. *Mol Aspects Med* 33(4):487–509.
63. Hu P, et al. (2013) Aryl hydrocarbon receptor deficiency causes dysregulated cellular matrix metabolism and age-related macular degeneration-like pathology. *Proc Natl Acad Sci USA* 110(43):E4069–E4078.
64. Malek G, et al. (2005) Apolipoprotein E allele-dependent pathogenesis: A model for age-related retinal degeneration. *Proc Natl Acad Sci USA* 102(33):11900–11905.
65. Luhmann UF, et al. (2009) The drusenlike phenotype in aging Ccl2-knockout mice is caused by an accelerated accumulation of swollen autofluorescent subretinal macrophages. *Invest Ophthalmol Vis Sci* 50(12):5934–5943.
66. Dithmar S, et al. (2001) Murine high-fat diet and laser photochemical model of basal deposits in Bruch membrane. *Arch Ophthalmol* 119(11):1643–1649.
67. Kliffen M, et al. (2000) The APO(*)E3-Leiden mouse as an animal model for basal laminar deposit. *Br J Ophthalmol* 84(12):1415–1419.
68. Picard E, et al. (2010) CD36 plays an important role in the clearance of oxLDL and associated age-dependent sub-retinal deposits. *Aging (Albany NY)* 2(12):981–989.
69. Imamura Y, et al. (2006) Drusen, choroidal neovascularization, and retinal pigment epithelium dysfunction in SOD1-deficient mice: A model of age-related macular degeneration. *Proc Natl Acad Sci USA* 103(30):11282–11287.
70. Justilien V, et al. (2007) SOD2 knockdown mouse model of early AMD. *Invest Ophthalmol Vis Sci* 48(10):4407–4420.
71. Hollyfield JG, et al. (2008) Oxidative damage-induced inflammation initiates age-related macular degeneration. *Nat Med* 14(2):194–198.
72. Weismann D, et al. (2011) Complement factor H binds malondialdehyde epitopes and protects from oxidative stress. *Nature* 478(7367):76–81.
73. Shaw PX, et al. (2012) Complement factor H genotypes impact risk of age-related macular degeneration by interaction with oxidized phospholipids. *Proc Natl Acad Sci USA* 109(34):13757–13762.
74. Clark SJ, et al. (2006) His-384 allotypic variant of factor H associated with age-related macular degeneration has different heparin binding properties from the non-disease-associated form. *J Biol Chem* 281(34):24713–24720.
75. Keenan TD, et al. (2014) Age-dependent changes in heparan sulfate in human Bruch's membrane: Implications for age-related macular degeneration. *Invest Ophthalmol Vis Sci* 55(8):5370–5379.
76. Prosser BE, et al. (2007) Structural basis for complement factor H linked age-related macular degeneration. *J Exp Med* 204(10):2277–2283.
77. Alexander JJ, Quigg RJ (2007) The simple design of complement factor H: Looks can be deceiving. *Mol Immunol* 44(1-3):123–132.
78. Wang L, et al. (2009) Lipoprotein particles of intraocular origin in human Bruch membrane: An unusual lipid profile. *Invest Ophthalmol Vis Sci* 50(2):870–877.
79. Dietzel M, et al. (2014) The contribution of genetic factors to phenotype and progression of drusen in early age-related macular degeneration. *Graefes Arch Clin Exp Ophthalmol* 252(8):1273–1281.
80. Clark SJ, et al. (2014) Identification of factor H-like protein 1 as the predominant complement regulator in Bruch's membrane: Implications for age-related macular degeneration. *J Immunol* 193(10):4962–4970.
81. Langford-Smith A, Keenan TD, Clark SJ, Bishop PN, Day AJ (2014) The role of complement in age-related macular degeneration: Heparan sulphate, a ZIP code for complement factor H? *J Innate Immun* 6(4):407–416.

82. Elner SG, et al. (2003) Human RPE cell apoptosis induced by activated monocytes is mediated by caspase-3 activation. *Trans Am Ophthalmol Soc* 101:77–89, discussion 89–91.
83. Yoshida A, et al. (2003) Activated monocytes induce human retinal pigment epithelial cell apoptosis through caspase-3 activation. *Lab Invest* 83(8):1117–1129.
84. Yang D, et al. (2007) Pro-inflammatory cytokines increase reactive oxygen species through mitochondria and NADPH oxidase in cultured RPE cells. *Exp Eye Res* 85(4): 462–472.
85. Yang D, et al. (2011) MCP-1-activated monocytes induce apoptosis in human retinal pigment epithelium. *Invest Ophthalmol Vis Sci* 52(8):6026–6034.
86. Hageman GS, et al. (2001) An integrated hypothesis that considers drusen as biomarkers of immune-mediated processes at the RPE-Bruch's membrane interface in aging and age-related macular degeneration. *Prog Retin Eye Res* 20(6):705–732.
87. Cherepanoff S, McMenamin P, Gillies MC, Kettle E, Sarks SH (2010) Bruch's membrane and choroidal macrophages in early and advanced age-related macular degeneration. *Br J Ophthalmol* 94(7):918–925.
88. Anand A, et al. (2012) Single nucleotide polymorphisms in MCP-1 and its receptor are associated with the risk of age related macular degeneration. *PLoS One* 7(11):e49905.
89. Despriet DD, et al. (2008) Comprehensive analysis of the candidate genes CCL2, CCR2, and TLR4 in age-related macular degeneration. *Invest Ophthalmol Vis Sci* 49(1):364–371.
90. Grunin M, Burstyn-Cohen T, Hagbi-Levi S, Peled A, Chowers I (2012) Chemokine receptor expression in peripheral blood monocytes from patients with neovascular age-related macular degeneration. *Invest Ophthalmol Vis Sci* 53(9):5292–5300.
91. Raoul W, et al. (2010) CCL2/CCR2 and CX3CL1/CX3CR1 chemokine axes and their possible involvement in age-related macular degeneration. *J Neuroinflammation* 7:87.
92. Combadière C, et al. (2007) CX3CR1-dependent subretinal microglia cell accumulation is associated with cardinal features of age-related macular degeneration. *J Clin Invest* 117(10):2920–2928.
93. Sennlaub F, et al. (2013) $CCR2^{+}$ monocytes infiltrate atrophic lesions in age-related macular disease and mediate photoreceptor degeneration in experimental subretinal inflammation in Cx3cr1 deficient mice. *EMBO Mol Med* 5(11):1775–1793.
94. Mattapallil MJ, et al. (2012) The Rd8 mutation of the Crb1 gene is present in vendor lines of C57BL/6N mice and embryonic stem cells, and confounds ocular induced mutant phenotypes. *Invest Ophthalmol Vis Sci* 53(6):2921–2927.
95. Hanna RN, et al. (2012) NR4A1 (Nur77) deletion polarizes macrophages toward an inflammatory phenotype and increases atherosclerosis. *Circ Res* 110(3):416–427.
96. Hilgendorf I, et al. (2014) Ly-6Chigh monocytes depend on Nr4a1 to balance both inflammatory and reparative phases in the infarcted myocardium. *Circ Res* 114(10): 1611–1622.
97. Kelly U, et al. (2010) Heparan sulfate, including that in Bruch's membrane, inhibits the complement alternative pathway: Implications for age-related macular degeneration. *J Immunol* 185(9):5486–5494.
98. Malagon F, Jensen TH (2011) T-body formation precedes virus-like particle maturation in *S. cerevisiae*. *RNA Biol* 8(2):184–189.
99. Pauleikhoff D, Sheraidah G, Marshall J, Bird AC, Wessing A (1994) [Biochemical and histochemical analysis of age related lipid deposits in Bruch's membrane.] *Ophthalmologe* 91(6):730–734. German.
100. Pauleikhoff D, Harper CA, Marshall J, Bird AC (1990) Aging changes in Bruch's membrane. A histochemical and morphologic study. *Ophthalmology* 97(2):171–178.
101. Holz FG, Sheraidah G, Pauleikhoff D, Bird AC (1994) Analysis of lipid deposits extracted from human macular and peripheral Bruch's membrane. *Arch Ophthalmol* 112(3):402–406.